Nuclear stopping and light charged particle emission in ^{12}C+^{12}C at 95 MeV/nucleon

G. Tian (田国玉), R. Wada, Z. Chen (陈志强), R. Han (韩瑞), W. Lin (林炜平), X. Liu (刘星泉), P. Ren (任培培), F. Shi (石福栋), F. Luo (罗飞), Q. Sun (孙琪), L. Song (宋林), and G. Q. Xiao (肖国青)

Phys. Rev. C **95**, 044613 — Published 21 April 2017

DOI: 10.1103/PhysRevC.95.044613

Nuclear stopping and Light charged particle emission in ^{12}C + ^{12}C at 95 MeV/nucleon

G. Tian(田国玉),[1,2] R. Wada,[3,1] Z. Chen(陈志强),[1,*] R. Han(韩瑞),[1] W. Lin(林炜平),[1] X. Liu(刘星泉),[1] P. Ren(任培培),[1,2] F. Shi(石福栋),[1] F. Luo(罗飞),[1] Q. Sun(孙琪),[1,2] L. Song(宋林),[1,2] and G. Q. Xiao(肖国青)[1]

[1]*Institute of Modern Physics, Chinese Academy of Sciences, Lanzhou 730000, China*

[2]*University of Chinese Academy of Sciences, Beijing, 100049, China*

[3]*Cyclotron Institute, Texas A&M University, College Station, Texas 77843*

(Dated: April 2, 2017)

Abstract

Detailed comparisons between the experimental data of ^{12}C + ^{12}C at 95 A MeV and transport model simulations are presented for all charged particles and fragments. For the simulations, AMD, a modified version of AMD (AMD-FM), and CoMD, are used. The experimental energy spectra and angular distributions are well reproduced by the AMD-FM calculations for light charged particles with $Z \leq 2$. We show that the nuclear stopping plays a key role for these observables. The production mechanisms of LCPs are discussed. The angular distributions of isotopes with $Z > 2$ are qualitatively reproduced reasonably well, but the yields are $2-10$ times smaller in the simulations for most isotopes.

PACS numbers: 25.70.Pq

*E-mail at: zqchen@impcas.ac.cn

I. Introduction

The $^{12}C + ^{12}C$ reaction at 95MeV/nucleon was performed at GANIL [1], motivated by the hadron beam therapy with Carbon ions to treat cancerous tumors. Angular distributions and energy spectra of ejectiles were compared with the reaction models embedded in the GEANT4 Monte Carlo toolkit [2]. In that comparisons, none of the toolkits provides good enough reproduction of the experimental data, especially for those from the intermediate velocity source. In order to improve the reproduction of the experimental data, they made further comparisons with an event generator, SLIIPIE (Simulation of Light Ions Induced Processes at Intermediate Energies) [3]. SLIIPIE is an event generator base on a participant-spectator model which is widely used at higher energy reactions. The production mechanism of particles is divided in two stages. In the first earlier stage, the production of light charged particles (LCPs) and fragments are treated. In the second stage, the sequential decay of excited fragments is treated. In each time stage, physics involved is parameterized with many free parameters. They were able to reproduce the experimental results rather well except for proton energy spectra at larger angles. In this article we focus on the physics for the production of these particles, comparing with transport model simulations. This is essential to improve our understanding of nuclear dynamics of heavy ion reactions and is one of the key objectives of contemporary nuclear physics.

In the intermediate energy heavy ion collisions (a few tens of MeV/nucleon to a few hundreds of MeV/nucleon), it is generally expected that the overlap region of the composite system of projectile and target nuclei is compressed and excited in the early stage of the reaction for central collisions, and then the hot-dense nuclear system expands and breaks up through multifragmentation processes. As experimental observables, the angular distributions and energy spectra of the emitted particles, influenced by the nuclear structure, nuclear mean filed and dynamics of collisions, play key roles for studying the transport mechanism of nucleons in nuclear reactions. In heavy ion collisions, nuclear stopping governs the dissipation of the kinetic energy and the collective motions, and reveals a variety of reaction mechanisms, such as multifragmentation, neck formation, and fusion reactions [4, 5].

Particle spectra at intermediate energy collisions have been empirically analyzed, using a moving source fit with three sources, projectile-like (PLF), intermediate velocity (IV) and target-like (TLF) sources [6–9]. The IV source has a source velocity of about a half projectile

velocity and a harder slope, comparing to those of PLF and TLF. Westfall et at., pointed out that the IV source of proton spectra can be described by a fireball model at incident energies above 200 MeV/nucleon [10]. The fireball model is commonly accepted for the production mechanism of the IV source of LCPs at the BEVALAC energy, based on the experimental data of the pioneering works at LBL [11, 12]. Below 200 MeV/nucleon, notable deviations from the fireball picture have been reported [10, 13, 14]. At energy below 10 MeV/nucleon, on the other hand, light particle emissions have been well described by fusion-evaporation scenario. At energies above 10 MeV/nucleon, pre-equilibrium emissions have been observed and they are consistent to a pre-equilibrium model based on the Boltzmann master equation [15–17]. Above 20 MeV/nucleron, the IV source of protons is also described reasonably by this scenario [8, 18].

In Ref. [19], Doré et al., presented a pioneering work for the emission of the IV source component of LCPs with a simplest microscopic model, using an intra-nuclear cascade (INC) code, followed by a percolation and an afterburner. They reproduced well the experimental parallel and transverse velocity distribution of LCPs in Ar + Ni at 95 MeV/nucleon. However, the multiplicity distributions of LCPs were poorly described by the model, especially for central collisions, indicating the interplay between the mean field dissipation and the in-medium nucleon-nucleon collisions becomes important. Wada et al., applied an antisymmetrized molecular dynamics (AMD) for ^{64}Zn + ^{58}Ni, ^{92}Mo, ^{197}Au at 26 to 47 MeV/nucleon and showed that AMD reproduces reasonably well the multiplicity and energy distributions of LCPs, including those of the intermediate mass fragments [20]. For light cluster emissions at intermediate energy domains, it has been shown that their energy spectra are well described by a thermal coalescence model [6, 7, 21]. A possible difference of the emission mechanisms for the IV source component of the protons and alpha clusters is suggested using a kinematical three body calculation in ^{32}S + Ag at 30 MeV/nucleon in Ref [22].

At the intermediate energy heavy ion collisions, energetic proton emissions of the IV component have been reported [23–25]. The proton energy exceeds more than four times of the incident projectile energy per nucleon. For the energetic proton emission we proposed a modified version of AMD, in which the Fermi boost is explicitly taken into account in the nucleon-nucleon collision process [26]. The new code is called AMD-FM. Using this new code, the experimentally observed energetic proton spectra from ^{40}Ar + ^{51}V at 44 MeV/nucleon [23] and those of ^{36}Ar + ^{181}Ta at 94 MeV/nucleon [25] are reproduced

reasonably well, without including an extra mechanism such as a three-body collision term or a short range correlation. An interesting fact in this calculations is that the Fermi boost newly installed in the code enhances the average number of Pauli-allowed collisions by about 40%, and modified the light particle angular distribution. We will see this effect below.

In order to further elucidate the production mechanism of LCPs at intermediate heavy ion collisions, we apply AMD [27–29], AMD-FM [26] and constrained molecular dynamics (CoMD) [30] to compare to the experimental angular distributions and energy spectra in the $^{12}C + ^{12}C$ reactions at 95 MeV/nucleon. The detailed comparisons reveal that the differences among these models in describing the production mechanism of charged light particles appear in these observables and enable us to constrain the models and their ingredients. The use of AMD for this work is its capability to reproduce the experimental isotope yields. AMD results, such as multiplicity, angular distributions and energy spectra, have often been compared with those from the experimental data in intermediate energy heavy ion collisions and reproduce them reasonably well [20, 27–29, 31–34].

II. Transport models

In this section, we briefly introduce the transport models (AMD, AMD-FM and CoMD) used in the presented work.

II-1. AMD

In AMD a reaction system with N nucleons is described by a Slater determinate of N Gaussian wave packets [35]

$$\Phi(Z) = \det\left\{ \exp\left[-\nu\Big(\boldsymbol{r}_j - \frac{\boldsymbol{Z}_i}{\sqrt{\nu}}\Big)^2 + \frac{1}{2}\boldsymbol{Z}_i^2 \right] \chi_{\alpha_i}(j) \right\} \tag{1}$$

where the complex variables $Z \equiv \{\boldsymbol{Z}_i; i = 1, \ldots, N\} = \{Z_{i\sigma}; i = 1, \ldots, N, \sigma = x, y, z\}$ represent the centroids of the wave packets. χ_{α_i} represents the spin and isospin states of $p\uparrow$, $p\downarrow$, $n\uparrow$, or $n\downarrow$. The width parameter ν is taken as $\nu = 0.16 fm^{-2}$, which is optimized to reproduce the experimental binding energy of nuclei properly. The experimental binding energies are reproduced within 10% for most nuclei [34]. The centroid of Gaussian wave

packets $\boldsymbol{Z}_i$ is given as

$$\boldsymbol{Z}_i = \sqrt{\nu}\boldsymbol{D}_i + \frac{i}{2\hbar\sqrt{\nu}}\boldsymbol{K}_i. \tag{2}$$

For a dilute nuclear gas system, $\boldsymbol{D}_i$ and $\boldsymbol{K}_i$ correspond to the position and momentum of each nucleon. However, those quantities do not have 1 to 1 correspondence to nucleons inside the nuclear system because of the antisymmetrization. Using the centroid of the Gaussian wave packets, the time evolution of $\boldsymbol{Z}_i$ is determined classically by the time-dependent variational principle and the two-body nucleon collision process. The equation of motion for Z is derived as

$$i\hbar \sum_{j\tau} C_{i\sigma,j\tau} \frac{dZ_{j\tau}}{dt} = \frac{\partial \mathcal{H}}{\partial Z^*_{i\sigma}}. \tag{3}$$

Here $\mathcal{H}$ is the Hamiltonian and $C_{i\sigma,j\tau}$ is a Hermitian matrix defined by

$$C_{i\sigma,j\tau} = \frac{\partial^2}{\partial Z^*_{i\sigma} \partial Z_{j\tau}} log\langle \Phi(Z)|\Phi(Z)\rangle. \tag{4}$$

In AMD, the centroid of the wave packet in the momentum space in the initial nuclei is set to nearly zero. This means that the initial nuclei are "frozen " and makes the initial nuclei stable in time.

AMD treats the nucleon-nucleon collision process in the physical coordinate space. The physical coordinate $W \equiv \{\boldsymbol{W}_i\}$ for a given nucleon, i, is defined as

$$\boldsymbol{W}_i = \sum_{j=1}^{A} (\sqrt{Q})_{ij} \boldsymbol{Z}_j \tag{5}$$

and Q_{ij} is defined as

$$Q_{ij} = \frac{\partial}{\partial (Z^*_i Z_j)} ln\langle \Phi(\boldsymbol{Z})|\Phi(\boldsymbol{Z})\rangle. \tag{6}$$

The Winger form of the ith nucleon at time $t = t_0$ is represented as

$$f_i(\boldsymbol{r}, \boldsymbol{p}, t_0) = 8 \exp\left\{ -2\nu(\boldsymbol{r} - \boldsymbol{R}_i(t_0))^2 - \frac{(\boldsymbol{p} - \boldsymbol{P}_i(t_0))^2}{2\hbar^2\nu} \right\} \tag{7}$$

with the centroid $\boldsymbol{R}_i$ and $\boldsymbol{P}_i$. The total one-body distribution function is the sun of f_i. This representation is valid only approximately when the physical coordinate

$$\boldsymbol{W}_i = \sqrt{\nu}\boldsymbol{R}_i + \frac{i}{2\hbar\sqrt{\nu}}\boldsymbol{P}_i \tag{8}$$

is used for the centroid [35]. In AMD calculations, similar to the other transport models, there are two important processes, one is the mean filed propagation of nucleons and the other is nucleon-nucleon (NN) collision process. In AMD, Pauli principle is fully respected in an exact manner in both processes. In the present work, the Gogny interaction [36] is used for the mean filed. The nucleon-nucleon cross section is given by [28]

$$\sigma(E,\rho) = min\left(\sigma_{LM}(E,\rho),\ \frac{100mb}{1+E/200MeV}\right) \tag{9}$$

where $\sigma_{LM}(E,\rho)$ is the cross section given by Li and Machleidt [37, 38].

Quantum fluctuation caused by the Fermi motion is taken into account in two ways. One is in the nucleon-nucleon collision process, described in the next subsection. The other is in the diffusion (and shrinking) process in the time evolution of the nucleon propagation. As described in details in the references, this process is taken into account in order to treat properly the multifragmentation process [28, 29]. In the present simulations, the version in Ref. [28] is used, in which the only diffusion process is taken into account. The time-dependent many-body wave function, described by Eq.(1) for complicated nuclear collisions, is a superposition of a huge number of channels, each of which corresponds to a different clusterization configuration. The time evolution in AMD described in Refs. [27, 28] is determined by two factors, the mean-field propagation and the decomposition into branches (quantum branching). The latter is treated numerically as follows. By simply introducing the parameter c and the normalized function $g(\xi)$, which depend on $\Phi[Z(t_0)]$, δt, and i, the diffusion of wave packets in one-body distribution function at $t = t_0 + \delta t$ can be written as a superposition of Gaussian functions as

$$f_i(x, t_0+\delta t) = (1-c)F[x - X_i(t_0+\delta t)] + c\int g(\xi)F[x - X_i(t_0+\delta t) - \xi]d\xi, \tag{10}$$

where

$$F(x) = \prod_{a=1}^{6}\sqrt{2/\pi}e^{-2x_a^2}, \tag{11}$$

$$x = \{x_a\}_{a=1,\ldots,6} = \left\{\sqrt{\nu}\boldsymbol{r}, \frac{\boldsymbol{p}}{2\hbar\sqrt{\nu}}\right\}, \tag{12}$$

$$X_i = \{X_{ia}\}_{a=1,\ldots 6} = \left\{\sqrt{\nu}\boldsymbol{R_i}, \frac{\boldsymbol{P}_i}{2\hbar\sqrt{\nu}}\right\}. \tag{13}$$

By restricting $g(\xi) \geq 0$ and $0 \leq c \leq 1$, the diffusion of the wave packets is described consistently. For more details about the quantum branching, we refer to Refs. [27, 28]. The

physical origin of the quantum branching is to take into account the quantum fluctuation in phase space as seen in the above formulation. The branching of wave packets to decomposed states originates from this fluctuation in the time evolution of the wave packets. Fermi boost taken into account in the two-body collision process as described in the next section originates from the same nucleon-nucleon interaction, but in AMD in Ref. [27] the diffusion process and the two-body collision process are treated as independent processes. Therefore we need to take into account the quantum fluctuation as the Fermi boost in both processes.

II-2. AMD-FM

AMD-FM is originally developed for describing the high energy proton spectra properly in intermediate heavy ion collisions [26]. However, as discussed below, it also results in increasing the nuclear stopping and making notable changes in the energy and angular distributions of the emitted particles.

In AMD-FM, the Fermi motion is taken into account in the two body collision process. When two nucleons are within the collision distance $\sqrt{\sigma_{NN}/\pi}$, the momentum uncertainty increases. This uncertainty of the momentum is given along the Gaussian distribution around the centroid of the Gaussian wave packets. This treatment is quite different from those in other transport models, in which the Fermi motion is given only once in the initial nuclei.

In the actual calculations for given coordinate vectors $\boldsymbol{r}_1$ and $\boldsymbol{r}_2$ of two attempted colliding nucleons, the associated momenta $\boldsymbol{P}_1$ and $\boldsymbol{P}_2$ are given as

$$\boldsymbol{P}_i = \boldsymbol{P}_i^0 + \Delta\boldsymbol{P}_i^{'} \qquad (i = 1, 2) \tag{14}$$

where $\boldsymbol{P}_i^0$ is the centroid of the Gaussian momentum distribution for the particle i and $\Delta\boldsymbol{P}_i^{'}$ is the Fermi momentum randomly given along the Gaussian distribution. Since the momentum distribution is partially taken into account in the wave packet propagation we subtract T_0 from $\Delta\boldsymbol{P}_i^{'}$ to avoid a double counting. T_0 is a mean energy for the Gaussian momentum distribution. For the Gogny interaction $T_0 = 9.20MeV$ is taken. After subtracting T_0, $\Delta\boldsymbol{P}_i^{'}$ is calculated as

$$\Delta\boldsymbol{P}_i^{'} = \sqrt{\left(\frac{|\Delta\boldsymbol{P}_i|^2}{2M_0} - T_0\right)2M_0}\frac{\Delta\boldsymbol{P}_i}{|\Delta\boldsymbol{P}_i|} \tag{15}$$

$$\Delta P_{i\tau} = \hbar\sqrt{\nu}(\rho_i/\rho_0)^{1/3}G(1) \tag{16}$$

where $G(1)$ is a random number generated along the Gaussian distribution with $\sigma = 1$. $(\rho_i/\rho_0)^{1/3}$ in Eq.(16) is used for taking into account the density dependence of the Fermi energy, ρ_i is the density at $\boldsymbol{r}_i$ and ρ_0 is the normal nuclear density. τ represents the x, y, z coordinates. When $|\Delta \boldsymbol{P}_i|^2/2M_0 < T_0$, $\Delta \boldsymbol{P}_i^{'}$ sets to zero.

When the collision is Pauli-blocked, the treatment in W space is canceled and the time evolution of wave packets continue in Z space. When the collision is Pauli-allowed, the momentum and energy conservations are restored. The energy restoration is achieved within the cluster, using the following equation.

$$\Delta E \ = \ \left(\sum_{i,\sigma} \frac{\partial \mathcal{H}}{\partial Z_{i,\sigma}} \ \cdot \ \frac{dZ_{i,\sigma}}{dt} \right) \Delta t. \tag{17}$$

where Δt is used as an artificial fine step for turning and $\mathcal{H}$ is the Hamiltonian of the cluster.

It is interesting to note that, in AMD, the width of the momentum distribution is determined from the uncertainty relation $\sigma_r \sigma_p = \hbar/2$ and $\sigma_r = 1/2\sqrt{\nu}$. This results in $\sigma_p = \hbar\sqrt{\nu}$. As mentioned earlier, ν is optimized as a free parameter to reproduce the experimental binding energy of nuclei and $\nu = 0.16 fm^{-2}$ is taken for the Gogny interaction. This ends up $\sigma_p = 78.9$ MeV/c, which is consistent to the value obtained by an analysis of the (e, e'p) experiment [39, 40].

II-3. CoMD

In the constrained molecular dynamics (CoMD) model, the calculation is based on a quantum molecular dynamics (QMD) model in which an additional Pauli-blocking process is taken into account in the time evolution of nucleons [30]. The additional constraint is made stochastically during the time evolution as follows. At each time step of the time evolution, the occupancy in phase space is calculated. If the occupancy value is more than 1, then the momentum of the overlapping nucleons is smeared in a small amount around the centroid until the occupancy becomes below 1. After the process, momentum and energy conservation are restored. A Skyrme interaction with a soft EOS is used for the effective interaction. Free NN-cross section is used with a cut off at low energy region. Different from AMD, in CoMD the Fermi motion is explicitly taken in the initial ground state nuclei. When the initial nuclei are prepared, the momentum is assigned to each nucleon under a local Fermi Gas assumption. In order to get enough stability during calculations with a

proper binding energy of these nuclei, the nuclei are further cooled by a friction method. Therefore the momentum distribution becomes much smaller values in the initial nuclei.

III. Results

In this section the comparisons between the simulated results and the experimental data are made. All simulated data have been treated for the secondary decay process, using Gemini++ [41], unless otherwise specified.

III-1. LCP

A. Moving source fit

As mentioned in the introduction, the energy spectra in intermediate energy heavy ion collisions can be described well by a moving source fit with three sources, that is, PLF, IV and TLF sources [6–9]. For the later discussions, we first perform a moving source characterization of LCP spectra to characterize the experimental energy spectra at different angles. Three moving sources are used, a PLF source with a velocity nearly beam velocity, an IV source with about a half beam velocity and a TLF source with a velocity close to zero. Each source has four parameters, multiplicity, energy slope (or temperature), Coulomb barrier, and source velocity. Typical results after optimizing these parameters for protons and ^{4}He particles at selected angles are shown in Fig. 1. For ^{4}He particles on the right column, each source dominates at specific angle(s), i.e., PLF dominates at 11° and the IV source at 19° and TLF at 41°. For protons on the left, the dominance of each source at a given angle becomes less distinct. The TLF source represents only the low energy part of the spectra at all angles measured. At 11° and 19°, PLF and IV sources dominate the major part of the spectra more or less equally. At 41° the spectrum is dominated by the IV source.

B. Angular Distribution

In this subsection the comparisons of angular distributions of LCPs are performed between the simulated results obtained from the three transport models and the experimental

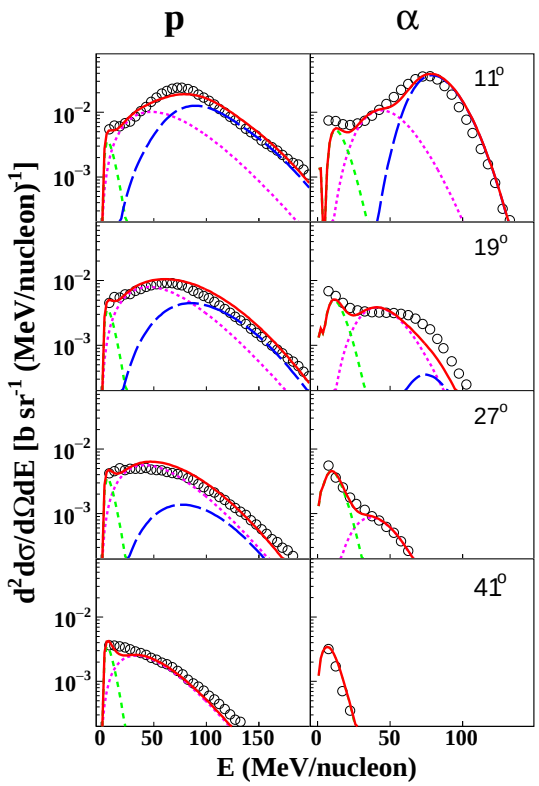

FIG. 1: (color online) Moving source fit results for protons on the left column and ^{4}He particles on the right. The experimental data from Ref. [1] are shown by open circles. PLF, IV and TLF components are shown by blue long-dashed, magenta dotted and green dashed lines, respectively. The total sum of the calculated spectra is shown by red solid lines. Theta lab. angles are shown in each figure.

data. In Figs.2-6, the first column on the left presents the angular distributions. The calculations are performed in the impact parameter range of b = 0-8 fm and the comparisons are made in an absolute scale. The experimental data are inclusive. In AMD, more than one million events are calculated up to $300 fm/c$ and Gemini++ is used as an afterburner. In Fig. 2, the results for protons are shown. CoMD simulation overpredicts the experimental cross sections at all angles. The AMD and AMD-FM simulations give better results. In Fig. 3, the calculated results for deuterons are compared to the experimental data. Contrary to protons, the CoMD simulation shows the best agreement with the experimental data. AMD and AMD-FM models overpredict the production of deuterons at forward angles. However, at larger angles only the AMD-FM results can reproduce the experimental angular distribution very well. For tritons in Fig. 4 CoMD underestimates the yield at all angles. The AMD and AMD-FM models overpredictsthe yield at forward angles, similar for

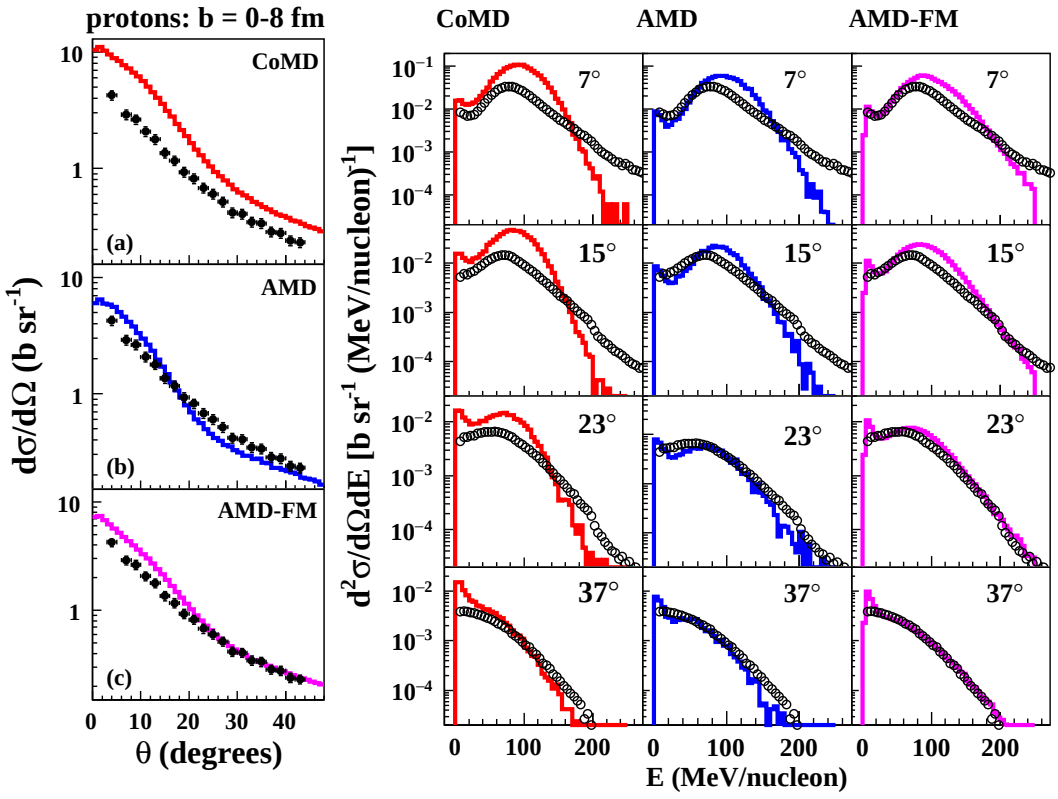

FIG. 2: (color online) Comparisons for proton angular distribution and energy spectra at selected angles with impact parameter b = 0-8 fm. The experimental data are shown by solid and open symbols. The calculated results of CoMD, AMD and AMD-FM are shown by red, blue and magenta solid histograms, respectively.

the case of deuterons, but the yields at angle $> 20°$ are more or less reasonably reproduced. In Fig. 5, the results for ^{3}He are shown. CoMD significantly underestimates the production at all angles, similar to the case for tritons. The AMD-FM results are very good at all angles. In Fig. 6, the results for ^{4}He particles are presented. The distributions obtained with the CoMD model are slightly better, comparing to those of the AMD and AMD-FM results at very forward angles. However, CoMD underestimates the ^{4}He production significantly at larger angles. Again AMD-FM reproduces the experimental yields at larger angles quite good.

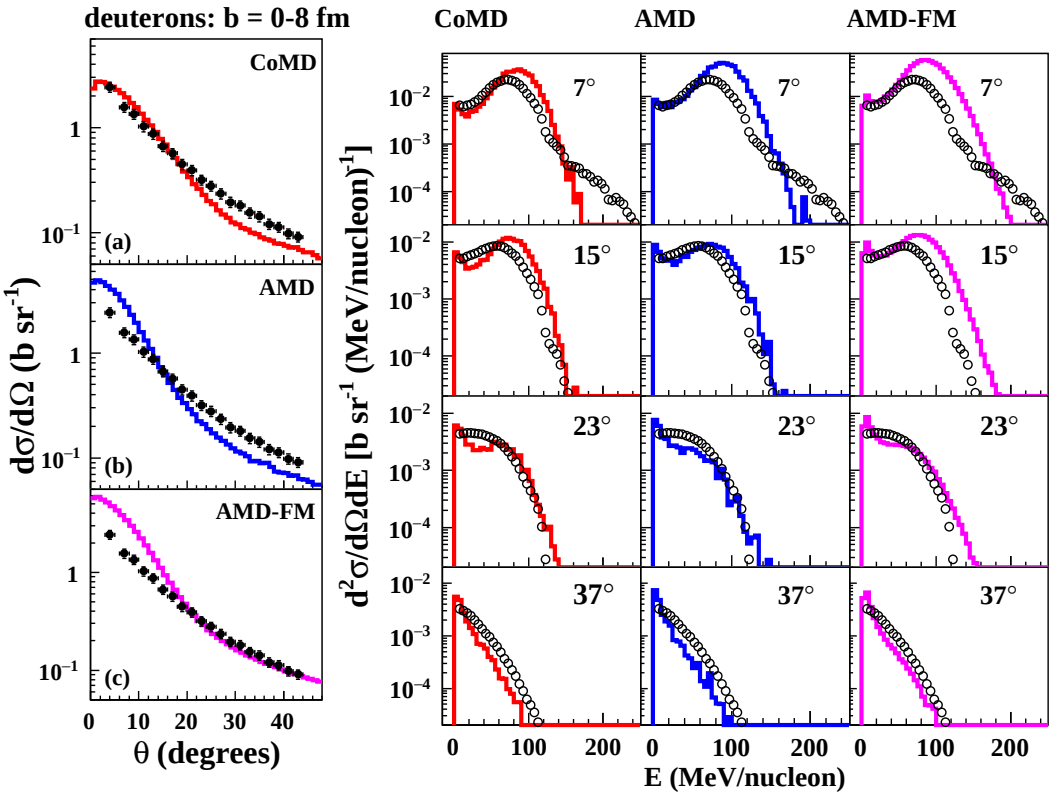

FIG. 3: (color online) Similar plot as Fig. 2, but for deuteron.

C. Energy Spectra

In this section we compare the experimental energy spectra with the simulations. In the published data in Refs. [2, 3], not only the cross section, but energy also has errors and this error exceeds more than $50MeV$ for protons at $E_p \sim 200MeV$. The error becomes smaller when the mass of the ejectiles becomes larger, as seen in the plots of Refs. [2, 3]. These large errors seem to originate from the energy calibration of Si detector in the Si-CsI telescopes, in which the total energy of LCPs is calculated from the energy loss in Si with a range-energy table. However as seen in Refs. [2, 3], the results of the GEANT4 and SLIIPIE simulations indicate that the energy calibration is reasonable, especially for protons. Our coalescence simulations described in the section IV-5, also support that their energy calibration is reasonable. Therefore in this paper we did not put any errors on the energy axis to avoid the misleading of the meaning of the errors, which is quite different from those of the cross section. The determination of the errors for the cross section is well described in Ref. [1]. In this section we use the moving source terminology, PLF, IV and

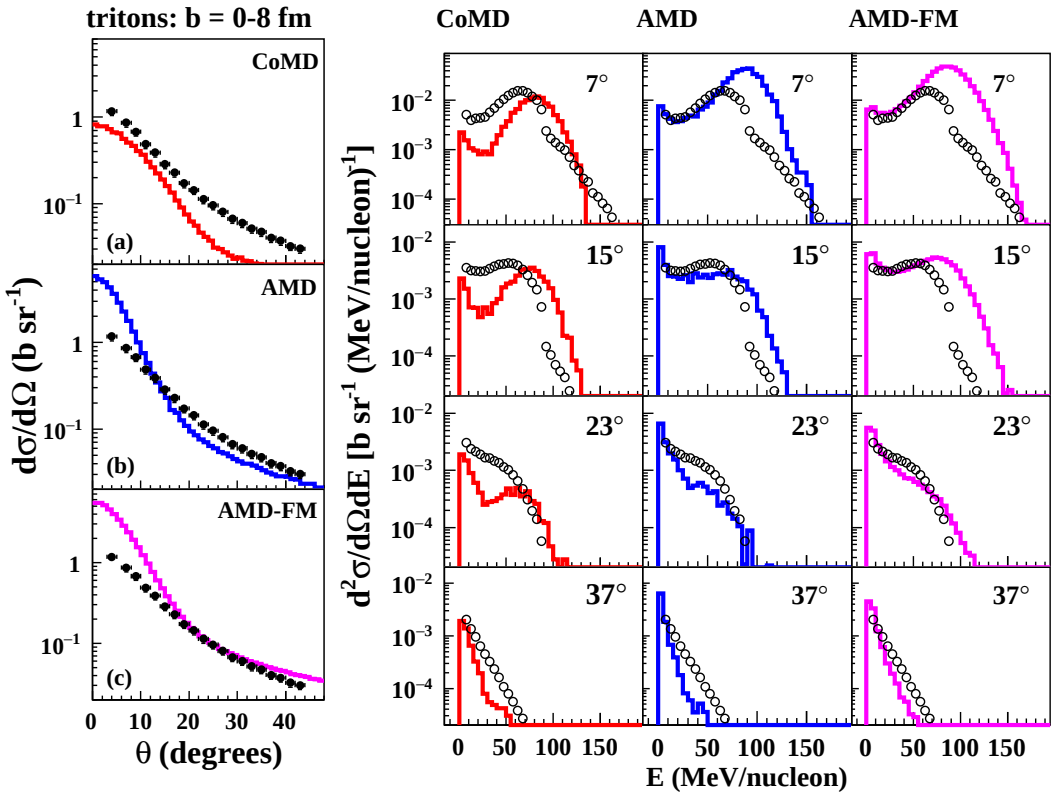

FIG. 4: (color online) Similar plot as Fig. 2, but for triton.

TLF described in the previous section, to discuss for the comparisons.

For protons, the AMD-FM simulation gives the best results among the three simulations, though the yield at $\theta = 7°$ and $15°$ are slightly overpredicted, which is dominated by the PLF component, whereas the spectra at $\theta \geq 23°$ are almost perfectly reproduced. All three calculations show an excess in the low energy region at $\theta \geq 15°$. This is caused by the TLF component and will be discussed later separately. For deuterons in Fig. 3, AMD and AMD-FM overpredict the PLF yield. The spectra at $\theta = 37°$ are underpredicted for all three simulations. Tritons are worst reproduced by simulations among other LCPs as shown in Fig. 4. The poor reproduction of the PLF component is partially caused by the experimental data themselves. It shows an unexpected drop off near $100 MeV/u$. AMD-FM reproduces the spectra at $\theta \geq 23°$ best. In Fig. 5, the results for ^{3}He are shown. For all calculations, the experimental data show significantly harder energy slopes at forward angles. For the spectra at $\theta \geq 23°$, AMD-FM does the best job to reproduce the spectra, but with slightly lower yield. In Fig. 6, the results for ^{4}He particles are presented. All three calculations show

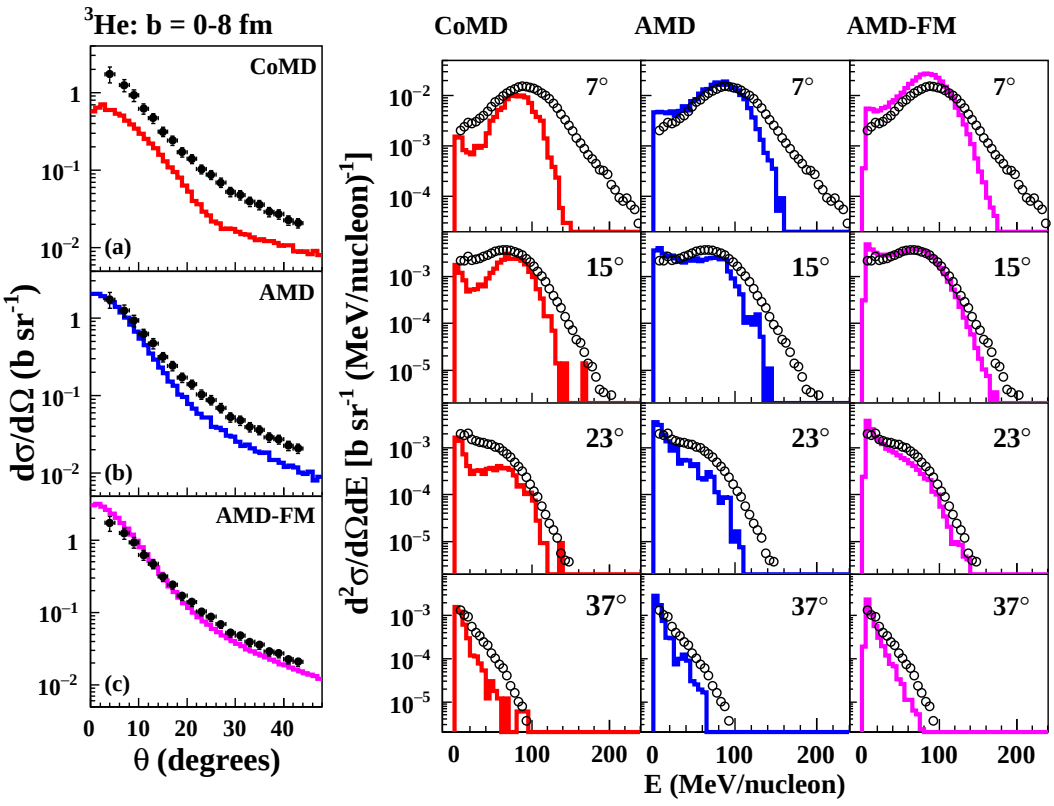

FIG. 5: (color online) Similar plot as Fig. 2, but for helium3.

the PLF peak energy slightly higher than that of the experimental data. Higher energy tail above 130 MeV at 7° in the experimental data is not observed at neighboring angles, indicating that it may be caused by some problems in the higher energy side of the spectrum at this angle. The IV yields at 15° are best reproduced by the AMD-FM simulation. The calculated TLF component at 37° shows a softer energy slope. The underprediction at larger angles does not show up in the angular distribution because of the overprediction of the TLF component at low energy. The enhancement of the low energy yields will be discussed in the section IV-4.

For the IV source component of the LCPs the energy spectra are best reproduced by the AMD-FM simulation. The IV source component originates from the overlap region between the projectile and target and exhibits most interesting characteristic with the highest temperature and density for the hot-dense nuclear matter study. Below, therefore, the AMD-FM results are further examined in details in the energy spectra.

In Fig. 7 the experimental energy spectra of LCPs are compared with those of the AMD-

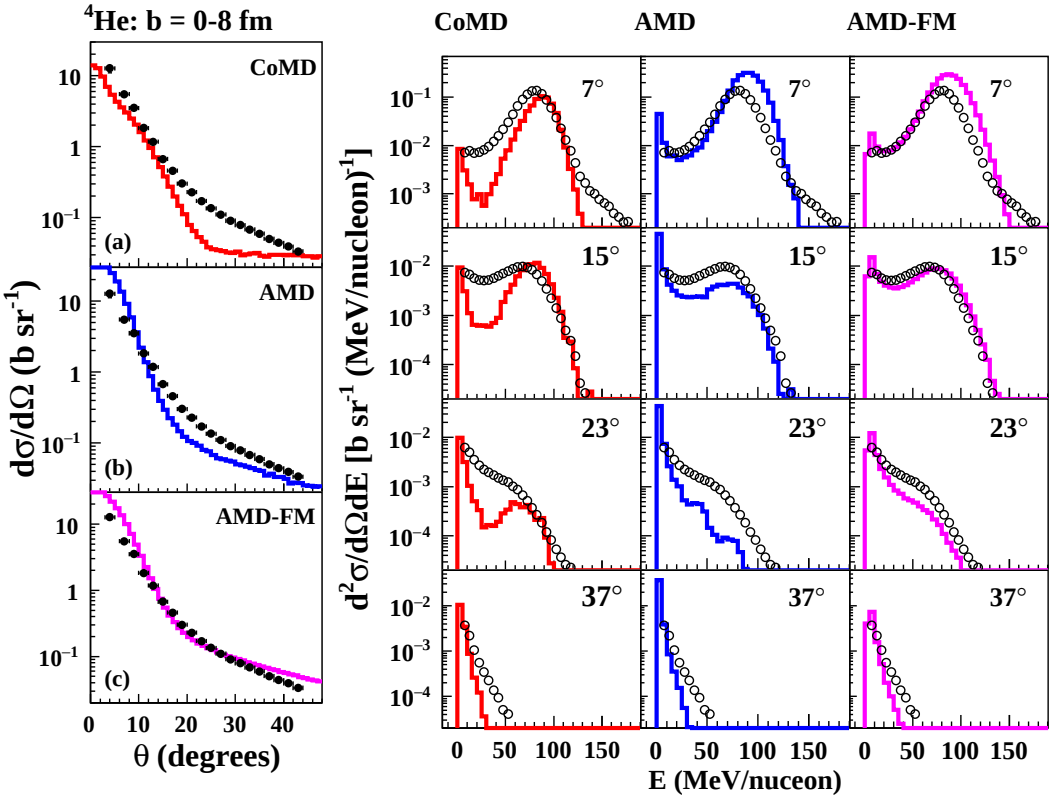

FIG. 6: (color online) Similar plot as Fig. 2, but for ^{4}He.

FM model predictions at different emission angles in an absolute scale. For comparisons at the entire available angles see also the Supplemental Materials [42] . Histograms in solid blue, dashed red and dotted green represent for total (AMD+Gemini), primary (AMD alone) and secondary (Gemini alone), respectively. In general, the secondary spectra (dotted green) show only two components, PLF and TLF.

For protons, the experimental PLF spectra at 11° show smaller yield, but harder slope than those of the AMD-FM simulations. The experimental spectra at $\theta \geq 19°$ are almost perfectly reproduced by the simulation. The TLF spectra at low energy for these angles are overpredicted by about a factor of two. This overprediction is observed for all particles in Fig. 7. For deuterons, the slopes of the IV component is well reproduced by the simulation, but the absolute cross sections are slightly overestimated at 13° and underpredicted at 43°. Similar results are obtained for tritons. For ^{3}He , on the contrary of the other LCPs, the contribution from the secondary decay process (green) is very small and the spectra are dominated from the primary emission from AMD at all angles. This improves the

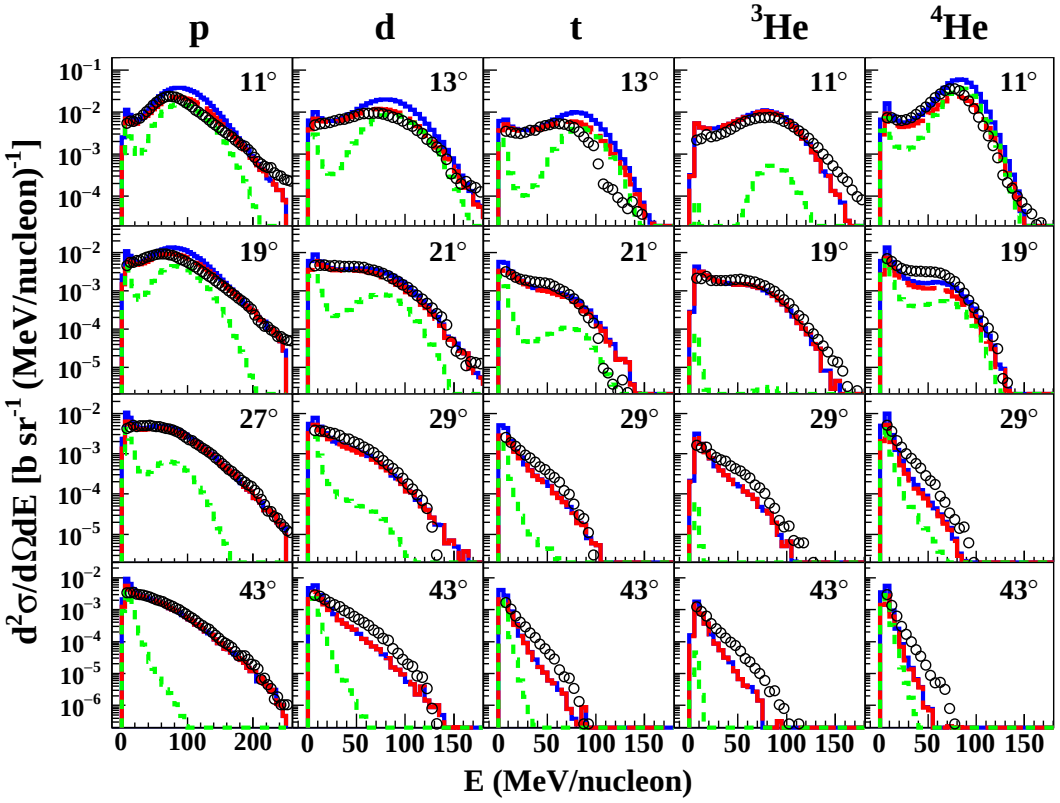

FIG. 7: (color online) Energy spectra of light charged particles at selected angles with impact parameter b = 0-8 fm. Experimental data are indicated by black circles. The red dashed histograms represent the particles generated from the primary hot nuclei, the green dotted histograms represent the particles from the secondary processes, and the blue solid histograms show the total particles.

reproduction of the PLF component by AMD-FM, though the experimental energy spectra of the PLF component show a slightly harder slope than that of the simulation. The spectra at $\theta \geq 29°$ are slightly underpredicted. Similar observation is made for ^{4}He particles at larger angles. For the PLF component, the simulation overpredicts, similar to other LCPs except for ^{3}He. For more detail comparisons of the energy spectra between ^{3}He and ^{4}He will be discussed in the section IV-2.

In summary, the PLF component of all LCP's are slightly overpredicted in yields by the simulation except for ^{3}He. For ^{3}He , the spectra are dominated by the primary process and the contribution from the secondary process is very small. The spectra of protons at larger angles are almost perfectly reproduced by the AMD-FM simulation, whereas for other LCPs, the velocity of the IV source in the simulated spectra is higher than that of the experimental

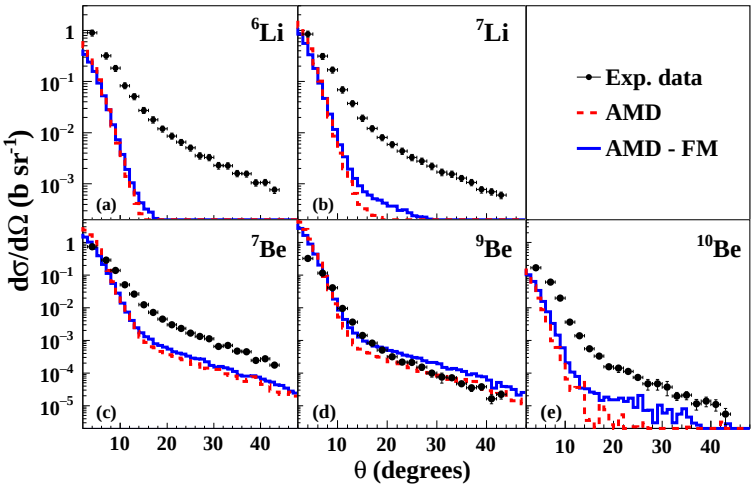

FIG. 8: (color online) Angular distributions for Li and Be isotopes. The experimental data are shown by solid points. The calculated results of AMD and AMD-FM are shown by red dotted and blue solid histograms, respectively.

spectra, and therefore the calculations underpredict the experimental yields at larger angles ($\theta > 30^\circ$). We will return this subject later.

III-2. IMF Angular distribution and Energy Spectra

Figs. 8 and 9 show the experimental angular distributions of various isotopes with $Z > 2$ together with those predicted by AMD (blue solid) and AMD-FM (red dashed histograms). The experimental data are shown by dots. The simulated angular distributions with AMD and AMD-FM are very similar each other at $\theta \leq 15^\circ$, but those of AMD-FM shows larger yields at larger angles by a factor of 2-10. The yields for Li isotopes are poorly reproduced by both simulations. For Be and C isotopes, the angular distributions show two component, one corresponds to the PLF and the other to the TLF source, as seen later in the energy spectra. For ^{9}Be, $^{10-11}$B and Carbon isotopes, the qualitative feature of the angular distribution is reasonably reproduced, but the yields are underestimated by a factor of 2-10. ^{9}Be is the best reproduced.

Fig. 10 shows the energy spectra for some isotopes with the AMD-FM simulations. At angles of 23° and 33°, since the experimental angular distributions show rather flat distributions at these angles, the spectra of 21° to 25° and of 31° to 35° are added to increase statistics and shown as those at 23° and 33°, respectively. The simulated yields are also

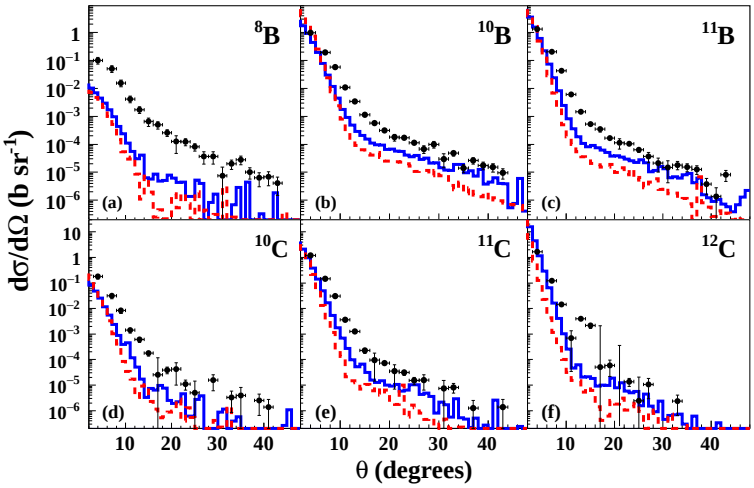

FIG. 9: (color online) Similar plot as Fig. 8

, but for B and C isotopes.

added accordingly. As shown in the figures, IMFs originate from two sources, PLF at the forward angles and TLF at larger angles. For ^{7}Li the spectra are dominated by the secondary emission, though the magnitude is more than 10 times smaller in the calculation. The contribution from the primary process increases as the mass increases and for ^{11}C, the primary products becomes comparable. There are no IV component is observed in the simulation. The angular distribution and energy spectra of only ^{9}Be are well reproduced in shape and yields.

IV. Discussions

IV-1. Impact parameter range

As shown in the previous sections, the yield of the PLF component is overpredicted for all particles except ^{3}He. Since the PLF component originates from peripheral collisions, the cross section of the PLF component is governed by the density distribution of the initial nuclei and collisions near the surface. For AMD simulations, the in-medium nucleon-nucleon(NN) cross section is calculated from the Li-Machleidt formulation. This formulation is used in the previous analysis of ^{64}Zn + ^{58}Ni, ^{92}Mo and ^{197}Au at 47 MeV/nucleon and light particle multiplicities and energy spectra are qualitatively well reproduced [20]. However, proton multiplicities are over-predicted by a factor of 1.7. In Ref [32], the approximation

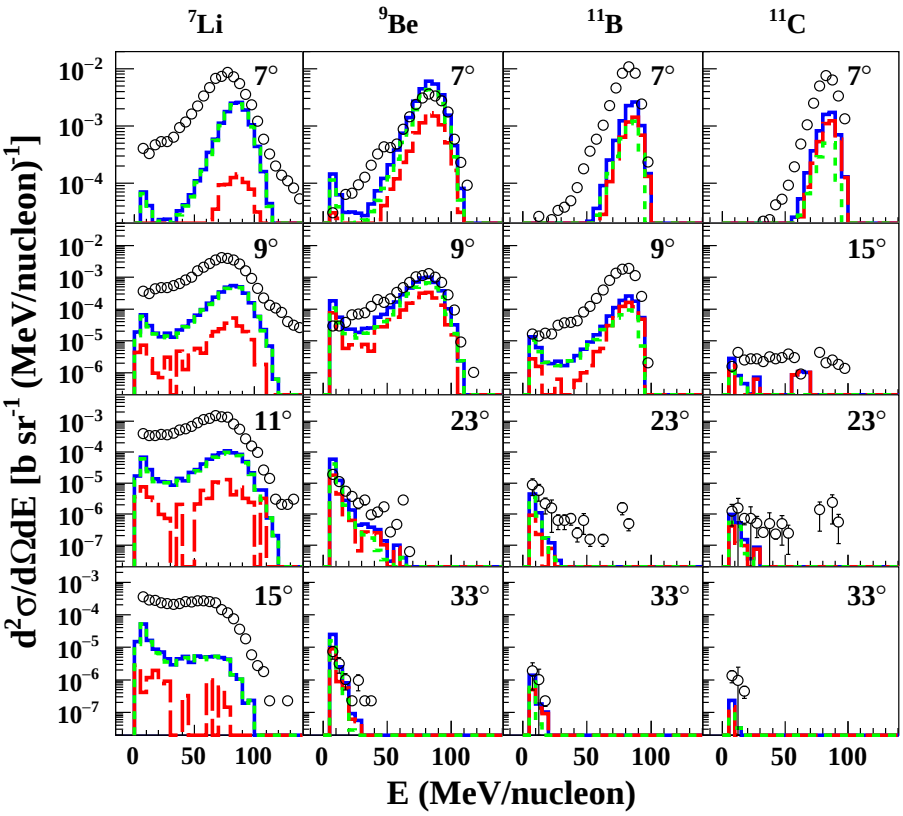

FIG. 10: (color online) Energy spectra of various isotopes at selected angles with impact parameter b = 0-8 fm. Experimental data are indicated by black circles. The red dashed histograms represent the particles generated from the primary hot nuclei, the green dotted histograms represent the particles from the secondary processes, and the blue solid histograms show the total particles.

for the physical coordinate in the AMD simulation is suggested for the cause of the excess yields.

As mentioned earlier, the physical coordinate expressed by Eq.(8) is reduced in an approximate manner and the physical coordinates tend to show a larger radius in the initial nuclei. In Fig. 11 the density distribution of the initial nucleus of ^{12}C is calculated in Z and W coordinates, and results are plotted as a function of the radius r, together with the experimental density distribution from Ref. [43]. The experimental distribution is calculated using the harmonic oscillator model parameters. In the figure the root mean square radius values, $< r >_{rms}$, are also given. The calculated density distribution from the Z coordinates show a slightly diffused distribution, comparing to that of the experimental one, but the calculated $< r >_{rms}$ (2.56 fm) is very close to that of the experimental value (2.46 fm). On

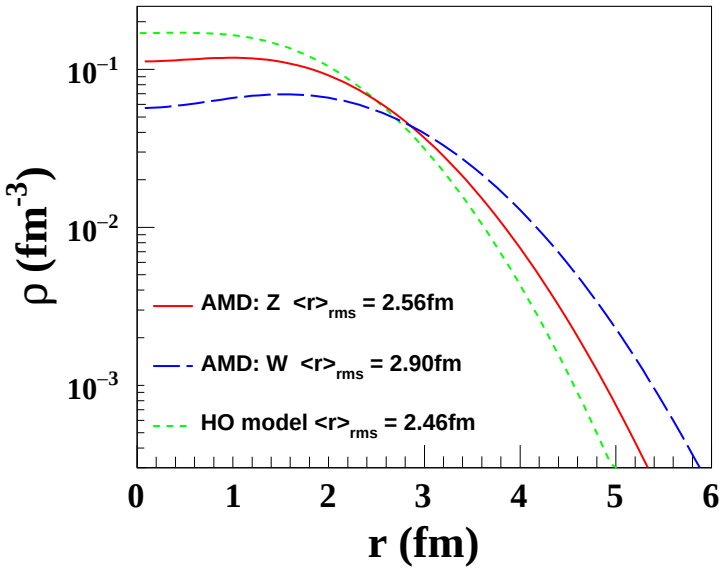

FIG. 11: (color online) Charge density distributions of ^{12}C. The solid curve is that of the initial nucleus calculated from the AMD coordinate Z_i. The dashed curve is the distribution calculated from the physical coordinate W_i. The dotted curve is the experimental density distribution from Ref.[43]. The root mean square radius values are also provided for each calculation.

the other hand the density distribution from the W coordinates is extended to much larger radius and the root mean square radius (2.90 fm) is much larger than those of the experiment and from the Z coordinates. In AMD the NN collisions probe the density distribution in the W coordinates and not in Z coordinates. Therefore the extended density distribution from the W coordinates eventually results in a significant increase of the number of collisions at large impact parameters, since the number of collisions is in proportion to the square of the nucleon number in the diffused region near the surface. This causes the increases of the excitation energy of the PLFs in peripheral events and enhances the secondary particle decay and eventually causes the overprediction of the PLF yields, observed in Fig. 7 for all particles except for ^{3}He. For ^{3}He, the secondary decay width is small, comparing other particle decay channels, and the PLF component is dominated by the primary process, which results in the good reproduction of the PLF component by AMD-FM + Gemini calculation.

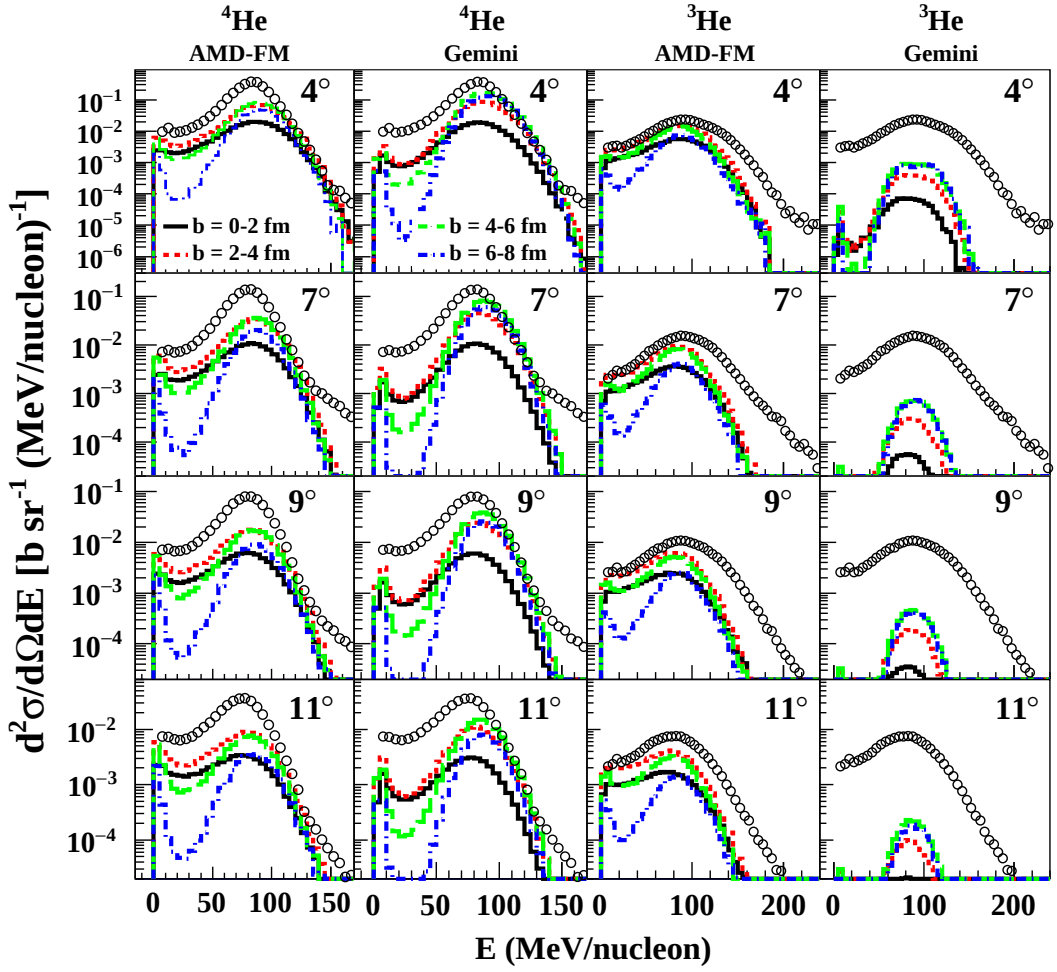

FIG. 12: (color online) Energy spectra of ^{4}He and ^{3}He at selected angles with impact parameter b = 0-2, 2-4, 4-6, and 6-8 fm, shown by black solid, red dotted, green dashed and blue dotted-dashed histograms, respectively. Inclusive data are indicated by black circles. First and third columns represent the primary products form AMD-FM. The second and fourth columns represent the particles generated from the secondary process.

IV-2. Production mechanism for ^{3}He

In Fig. 12, the energy spectra of ^{3}He and ^{4}He particles are compared between the experimental data and the simulations (histograms) at forward angles. In the first and third columns the experimental data are compared with the primary products from the impact parameters b = 0-2, 2-4, 4-6, and 6-8 fm separately. In the second and fourth columns, the secondary products from Gemini are plotted. For ^{4}He particles, one can see significant contributions from the secondary process (Gemini) at the impact parameter $b > 2fm$. On

the other hand, for ^{3}He, the yields from the secondary process is suppressed at all impact parameter ranges. The contributions from the primary process in the spectrum shape and in the different impact parameter ranges do not differ much between ^{4}He and ^{3}He, indicating that the difference observed moving source analysis in the literature [8, 21] originates from the difference of the contribution from the secondary decay process in the energy spectra. In Ref. [45] they demonstrated that the 3α cluster structures in ^{12}C nucleus below the excitation energy $E_x < 15$MeV are well taken care of in the AMD simulations and ^{4}He particles from these states make significant contributions to the energy spectra at the primary stages. These contributions have been observed as a moderate enhancement of the primary yield of ^{4}He particles, comparing to that of ^{3}He as seen in the first and third columns of Fig. 12.

IV-3. Nuclear stopping

In Fig. 13, the number of attempted and Pauli-allowed collisions are plotted as a function of time. About 50-60% of attempted collisions are blocked near the peak at 40fm/c and about 80% are blocked after 100fm/c. The number of Pauli-allowed collisions of AMD-FM calculation slightly increase by comparing to those of the AMD calculation. This increases enhances the nuclear stopping and affects the angular and energy distributions of the emitted particles. In Fig. 14 the comparison of nuclear stopping is made for AMD and AMD-FM calculations. To quantify the nuclear stopping power following to Refs. [4, 5], the energy-based isotropy ratio R_E, which is the ratio of the transverse energy to the parallel energy, is defined as

$$R_E = \frac{\sum E_\perp}{2\sum E_\parallel} \tag{18}$$

where $E_\perp(E_\parallel)$ is the transverse (parallel) energy in the center-of-mass (c.m.) system. As shown in the figure, one can see the small, but clear increase of the nuclear stopping in the AMD-FM simulations.

IV-4. Enhancement of low energy LCP spectra

As mentioned related to Fig. 7, a clear enhancement of the yields in the low energy side is observed in the AMD-FM simulations. In Fig. 15, energy spectra of LCPs at 23° are plotted

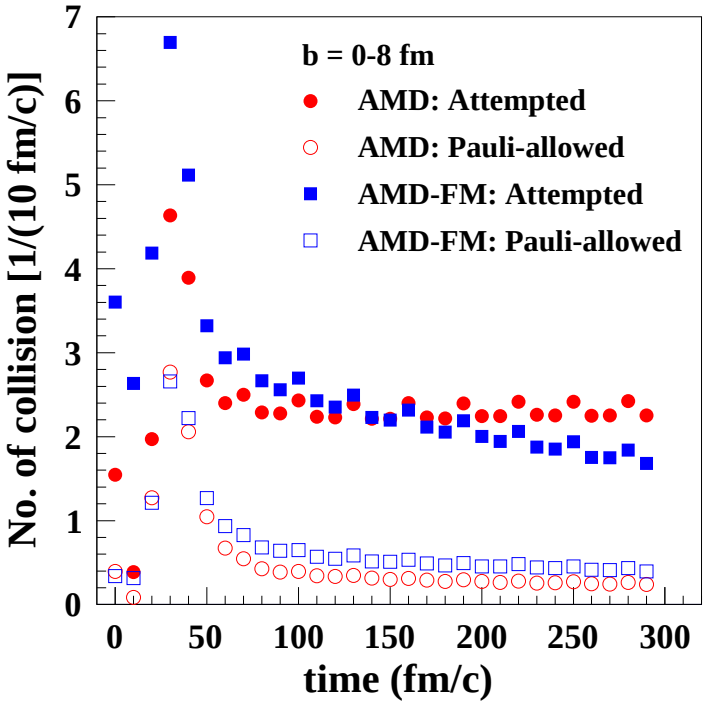

FIG. 13: (color online) The number of attempted and succeed collisions as a function of time. Counts are for every 10fm/c time interval.

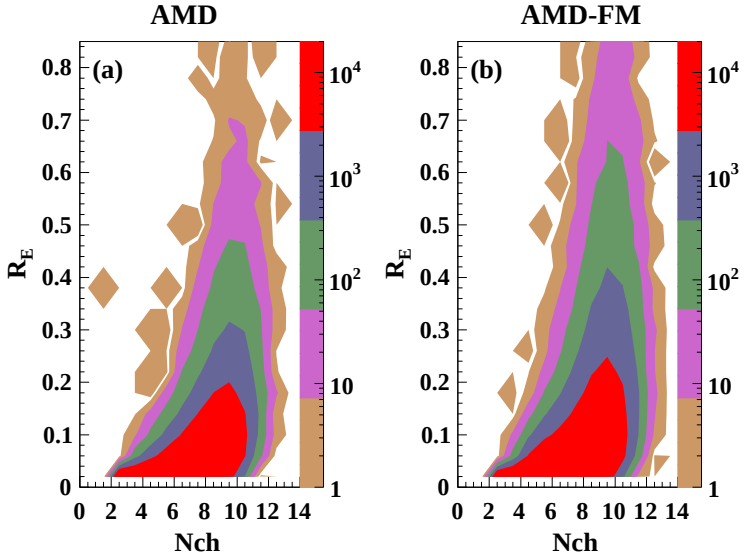

FIG. 14: (color online) Nuclear stopping from two models with the impact range $0 \leq b < 8fm$.

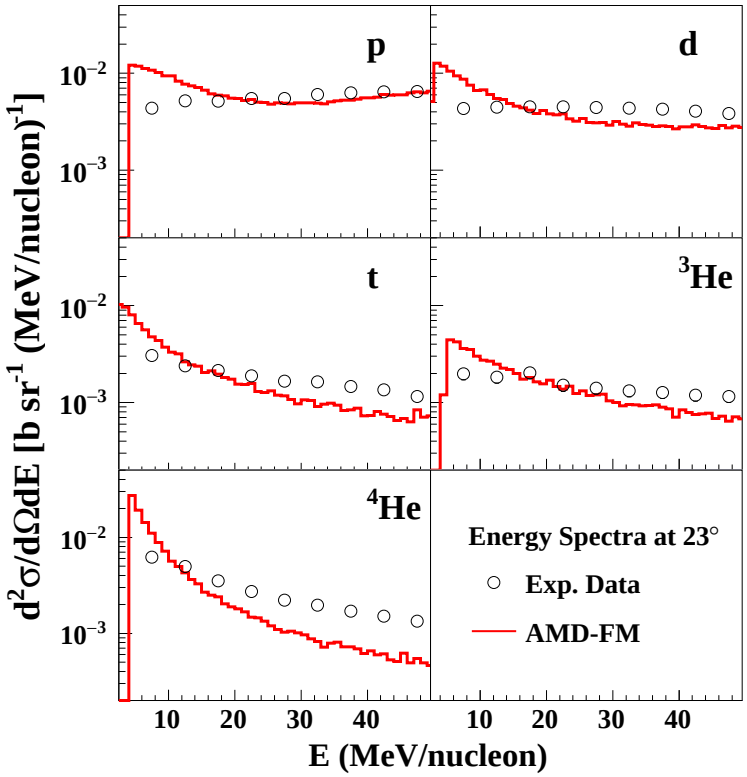

FIG. 15: (color online) Energy spectra of light charged particles at 23°. Open circles: experimental data. Red histograms: results of AMD-FM model.

in the energy range $0 < E < 50MeV$. As one can see the enhancement of the simulations occurs below or near the experimental energy threshold although they are not specified in Ref. [1]. Since the reaction of ^{12}C + ^{12}C is a symmetric system, the overprediction of the low energy yields partially corresponds to the overprediction of the PLF component discussed above except for ^{3}He.

IV-5. Coalescence model analysis

The coalescence approach has been often applied at relativistic heavy ion collisions under the no Coulomb assumption. At intermediate energies the assumption may not be acceptable. For example, while Coulomb force can be typically ignored at relativistic energies, Awes et al. [6] have shown that they must be taken into account in the energy range which is considered here. Therefore, to determine the coalescence parameter P_0 form the experimental data we follow the Coulomb corrected coalescence model formalism of Awes

et al. [6]. In the laboratory frame the derived relationship between the observed cluster and proton differential cross section is

$$\frac{d^2N(Z,N,E_A)}{dE_A d\Omega} = R_{np}^A \frac{A^{-1}}{N!Z!}\left\{\frac{\frac{4}{3}\pi P_0^3}{[2m^3(E-E_c)]^{1/2}}\right\}^{A-1} \times \left[\frac{d^2N(1,0,E)}{dEd\Omega}\right]^A, \qquad (19)$$

where the double differential multiplicity for a cluster of mass number A, containing Z protons and N neutrons. Coulomb-corrected energy E_A is related to the proton double differential multiplicity at the same Coulomb corrected energy per nucleon $E - E_c$, where E_c is the Coulomb barrier for proton emission. $R_{np}^A = [(N_t + N_p)/(Z_t + Z_p)]^A$ is the invariant coalescence factor where N_t, N_p and Z_t, Z_p are the neutron and proton numbers of target and projectile respectively. m is the nucleon rest mass. The double differential multiplicity for a given event is not a measured quantity. Therefore it is approximated by the average differential multiplicity

$$\frac{d^2N(Z,N)}{dE_A d\Omega} = \frac{1}{\sigma_R}\frac{d^2\sigma(Z,N)}{dE_A d\Omega} \qquad (20)$$

where σ_R is the total reaction cross section. In Fig. 16, the energy spectra of the composite light particles (black solid points) are compared with the calculations. P_0 values are calculated individually at each angle and the extracted values are plotted by symbols in Fig. 17. For all the cases, the values increase as the angle becomes larger and becomes flat distribution at angle around $25^\circ - 30^\circ$. We interpret this behavior as the interplay between the PLF and IV components. At small angles, the PLF component dominates, which have smaller P_0 values, comparing to those of the IV source. When the angle becomes larger, the IV source components contribute more to the energy spectra and they start to dominate at $\sim 25 - 30^\circ$. For the P_0 value of the IV source, the values at $\theta \geq 25^\circ$ are averaged over and indicated by dashed line in the figure. The calculated spectra from the individual fit are presented by red circles and those for the IV source average values are shown by blue squares.

In overall the coalescence model calculations reproduce very well for the IV source component. For the PLF component of deuterons and ^{4}He particles, the spectra are rather well reproduced. This is because in the PLF component of p, d and ^{4}He particles, the yields from the sequential decay process dominates, that is, the production mechanisms are similar. This may be also true for the tritons, but the experimental data seem having some problems at forward angles. On the contrary for ^{3}He as discussed above, the experimental spectra

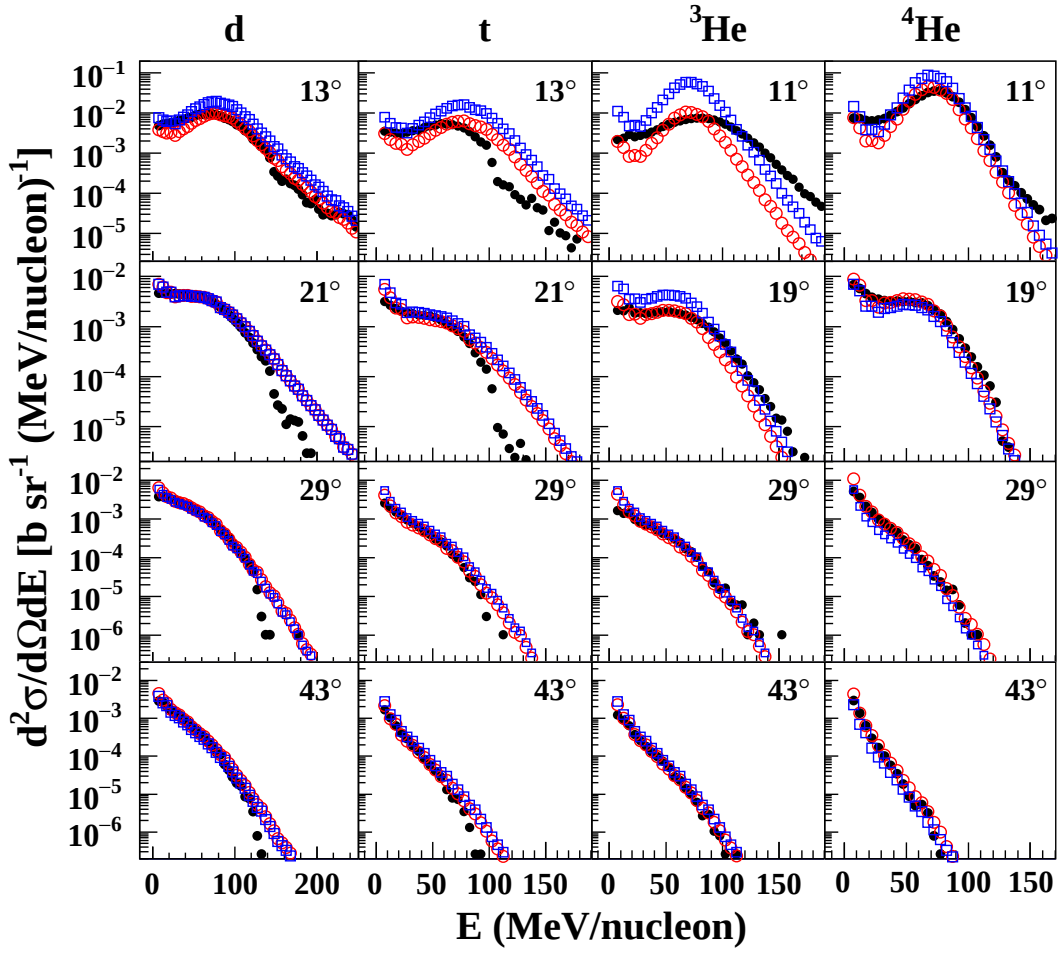

FIG. 16: (color online) Energy spectra of deuterons, tritons, ^{3}He, and ^{4}He particles at selected angles. Experimental data are indicated by black solid points. The red open circles and blue open squares are spectra predicted by the individual fit P_0 and average P_0 of the coalescence model of Eq.(19), respectively.

are dominated by the primary products and therefore coalescence model does not work well, supporting the conclusion that made in the section IV-2. Almost perfect reproduction of the IV source component with a single average P_0 value for each LCP indicates that these particles are generated by the coalescence mechanism, even for the ^{4}He particles.

The significant difference of the P_0 values for ^{4}He and other LCPs at smaller angles indicates that there a significant difference in the production mechanism for the PLF component between ^{4}He and other LCPs. The energy spectra shown in Fig. 7 indicate that this difference originates from the exhibition of the alpha cluster structure in ^{12}C nuclei when they are excited below 10-15MeV [44, 45]. In our analysis, the P_0 values for ^{4}He and deuterons show a similar value for the IV component, which is distinct contract to those of other analysis,

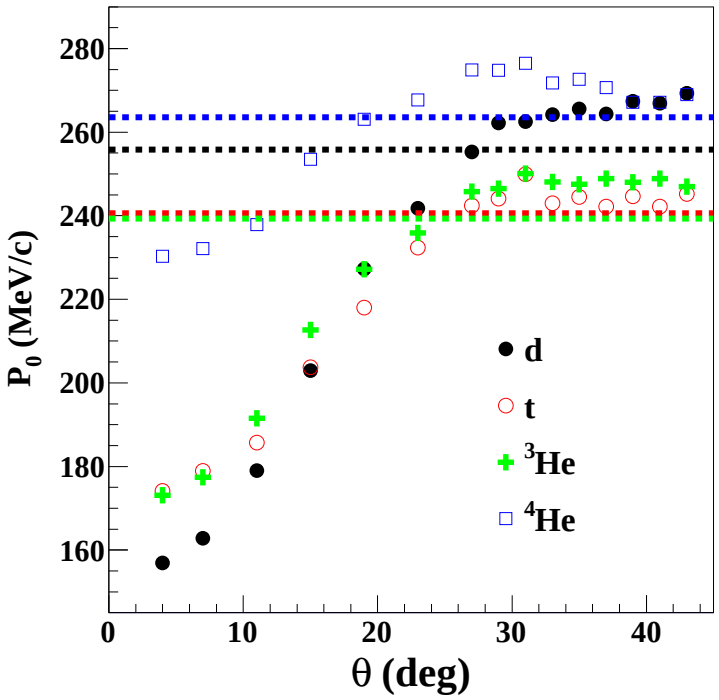

FIG. 17: (color online) The extracted values of P_0 as a function of outgoing angles in the lab system. The open and solid points show the results by individual fit and the dash lines present the average P_0 used for the coalescence calculations.

such as those of ^{40}Ar + ^{112}Sn at 47 MeV/nucleon [46] and ^{16}O + ^{197}Au at 310 MeV/nucleon [7]. In these references, deuterons show smaller P_0 values, reflecting the weak binding and therefore a possible large spread of nucleons in the deuterons. In our analysis, this effect is not observed.

V. Summary

The angular distributions and energy spectra of all ejectiles from the ^{12}C + ^{12}C reactions at 95MeV/nucleon of Ref. [1] are studied, comparing to the three transport model calculations. In overall AMD-FM reproduces best the experimental data, which results from the slightly larger nuclear stopping, originating from the increase of the Pauli allowed NN collisions in the collision process with the newly installed Fermi boost in AMD-FM. The success of the coalescence model calculations for the IV source component of LCPs indicates that these particles are mainly produced by the coalescence mechanism from the overlap region

of hot-dense nuclear matter generated between the projectile and the target during the early stage of the collisions. ^{3}He shows that the contribution from the sequential decay process is very small in the energy spectra and this causes a distinct difference in the PLF component, comparing other LCPs.

AMD is a very cpu time demanding program and the required CPU time increases approximately in proportion to A^3 where A is the system size. However for a small reaction system, such as $^{12}C + ^{12}C$ in this study, the required CPU time is about 2.5 times for AMD and 3.5 times for AMD-FM, comparing to that of CoMD calculation. Using a PC with Intel core-i7 4790k processor (4 cores 8 cpus), it takes about 2.5 min/cpu for 10 events in AMD simulations. Therefore for studies of the hadron beam therapy, motivated the original experiments in GANIL, AMD can be one of physics modules in the GEANT toolkit for more accurate simulations, which is crucial for such medical applications.

Acknowledgments

We thank A. Ono for providing his AMD code. This work is supported by the National Natural Science Foundation of China (Grant Nos. 11075189, 91426301 and 11605257) and the Strategic Priority Research Program of the Chinese Academy of Sciences "ADS project" (Grant No. XDA03030200). This work is also supported by the US Department of Energy under Grant No. DE–FG02–93ER40773. One of the authors (R.W) thanks the program of the "visiting professorship of senior international scientists of the Chinese Academy of Sciences" for their support during his stay in IMP.

[1] J. Dudouet et al., Phys. Rev. C **88**, 024606 (2013); http://hadrontherapy-data.in2p3.fr.

[2] J. Dudouet, D. Cussol, D. Durand, and M. Labalme, Phys. Rev. C **89**, 054616 (2014).

[3] J. Dudouet and D. Durand, Phys. Rev. C **94**, 014616 (2016).

[4] G. Lehaut, D. Durand et al. (INDRA and ALANDIN Collaborations), Phys. Rev. Lett. **104**, 232701 (2010).

[5] O. Lopez et al., Phys. Rev. C **90** 064602 (2014).

[6] T. C. Awes et al., Phys. Rev. C **24**, 89 (1981).

[7] T. C. Awes et al., Phys. Rev. C **25**, 2361 (1982).

[8] R. Wada et al., Phys. Rev. C **39**, 497 (1989).

[9] G. D. Westfall et al., Plys. Lett. B **116** 118 (1982).

[10] G. D. Westfall et al., Phys. Rev. C **29** 861 (1984).

[11] G. D. Westfall et al., Phys. Rev. Lett **37** 1202 (1976).

[12] Gosset et al., Phys. Rev. C **16** 629 (1977).

[13] T. Lefort et al., Nucl. Phys. A **662** 397 (2000).

[14] D. Dor*é* et al., Phys. Lett, B **491** 15 (2000).

[15] M. P. Kelly et al., Phys. Rev. C **56**, 3201 (1997).

[16] J. G*ó*mez del Campo et al., Phys. Rev. C **60**, 021601 (1999).

[17] J. Cabrera et al., Phys, Rev. C **68**, 034613 (2003).

[18] Cervesato et al., Phys. Rev. C **45** 2369 (1992).

[19] D. Dor*é* et al., Phys. Rev. C **63** 034612 (2001).

[20] R. Wada et al., Phys. Rev. C **69**, 044610 (2004).

[21] K. Hagel et al., Phys. Rev. C **62** 034607 (2000).

[22] R. Wada et al., Nucl. Phys. A **539** 316 (1992).

[23] R. Coniglione et al., Phys. Lett. B **471**, 339 (2000).

[24] P. Sapienza et al., Phys. Rev. Lett **87**, 072701 (2001).

[25] M. Germain et al., Nucl. Phys. A **620**, 81-90 (1997).

[26] W. Lin et al., Phys. Rev. C **94** 064609 (2016).

[27] A. Ono and H. Horiuchi, Phys. Rev. C **53**, 2958 (1996).

[28] A. Ono, Phys. Rev. C **59**, 853 (1999).

[29] A. Ono, S. Hudan, A. Chbihi, and J. D. Frankland, Phys. Rev. C **66**, 014603 (2002).

[30] M. Papa, T. Maruyama, and A. Bonasera, Phys. Rev. C **64**, 024612 (2001).

[31] R. Wada et al., Phys. Lett. B**442**, 6 (1998).

[32] R. Wada et al., Phys. Rev. C **62**, 034601 (2000).

[33] S. Hudan, T. de Souza, and A.Ono, Phys. Rev. C **73**, 054602 (2006).

[34] A. Ono, and H. Horiuchi, Prog. Part. Nucl. Phys. **53**, 501 (2004).

[35] A. Ono, H. Horiuchi, Toshiki Maruyama, and A. Ohnishi, Prog. Theor. Phys. **87**, 1185 (1992).

[36] J. Dechargé and D. Gogny, Phys. Rev. C **21**, 1568 (1980).

[37] G. Q. Li and R. Machleidt, Phys. Rev. C **48** 1702 (1993).

[38] G. Q. Li and R. Machleidt, Phys. Rev. C **49** 566 (1994).

[39] I. Bobeldijk et al., Phys. Rev. Lett. **73**, 2684 (1994).

[40] I. Bobeldijk et al., Phys. Lett. B **353**, 32 (1994).

[41] R. Charity, Phys. Rev. C **82**, 014610 (2010).

[42] See Supplemental Material at [URL will be inserted by publisher] for comparisons between AMD-FM and the experimental LCP spectra at the entire available angles.

[43] C. W. De Jager, H. De Vries and C. De Viries, Atom. Data Nucl.Data Tabl. 14, 479, (1974).

[44] O. S. Kirsebom et al., Phys. Rev. C **81**, 064313 (2010).

[45] H. Takemoto, H. Horiuchi, and A. Ono, Phys. Rev. C **57**, 811 (1998).

[46] R. Wada et al., Phys. Rev. C **85** 064618 (2012).